Research Square

Preprints are preliminary reports that have not undergone peer review.
They should not be considered conclusive, used to inform clinical practice,
or referenced by the media as validated information.

Large-Eddy Simulation of Momentum Balance, Internal Boundary Layer Development, and Turbulent Flow Adjustment Across a Canopy-to-Clearing Transition

Luis Aramis R. Pinheiro

aramisrp@gmail.com

Universidade de Brasília

Rafael Castilho Faria Mendes

Universidade de Brasília

Mário Benjamim Baptista de Siqueira

Universidade de Brasília

Antônio César Pinho Brasil Jr

Universidade de Brasília

Research Article

Keywords: Canopy-clearing transitions, Large-eddy simulation, Internal boundary layer, Turbulent momentum budget, Shear length scale, Vegetation-atmosphere interaction, Roughness transition, Momentum budget closure, Shear layer relaxation

Posted Date: November 12th, 2026

DOI: https://doi.org/10.21203/rs.3.rs-11283706/v1

License: This work is licensed under a Creative Commons Attribution 4.0 International License.
Read Full License

Additional Declarations: No competing interests reported.

Large-Eddy Simulation of Momentum Balance, Internal Boundary Layer Development, and Turbulent Flow Adjustment Across a Canopy-to-Clearing Transition

Luis Aramis R. Pinheiro[1*], Rafael C. F. Mendes[1†], Mário B. de Siqueira[1†], Antonio C. P. Brasil Jr[1†]

[1*]Energy and Environmental Laboratory, Mechanical Engineering Department, University of Brasília, Campus Universitário Darcy Ribeiro, Brasília, 70910-900, Federal District, Brazil.

*Corresponding author(s). E-mail(s): aramisrp@gmail.com;
Contributing authors: rafael.mendes@unb.br; mariosiqueira@unb.br; brasiljr@unb.br;
[†]These authors contributed equally to this work.

Abstract

Abrupt canopy-to-clearing transitions generate internal boundary layers and non-equilibrium turbulence that govern surface momentum exchange. Large-eddy simulations of a canonical wind-tunnel canopy-to-clearing case use a localized dynamic kinetic-energy sub-grid model with vertically distributed canopy drag. Inside the canopy, simulated mean velocity and friction velocity agree closely with particle image velocimetry and hot-wire anemometry (RMSE $\mathbf{0.141}$ for $\overline{u}/U_h$ and $\mathbf{0.043}$ for $\overline{u}/U_0$; Table 3). Above the crest, the continuous porous medium over-predicts Reynolds shear stress (RMSE $\mathbf{0.395}\,u_*^2$) and streamwise variance, consistent with homogenized stem-wake effects. At sub-canopy height, advection, pressure gradients and Reynolds-stress divergences peak within five canopy heights of the edge and keep turbulent stresses elevated to $x/h \approx 20$. Including the sub-grid stress divergence lowers the momentum residual to $|R_x| < 0.03$ beyond $x/h \approx 10$; closer to the edge, dispersive stresses from unresolved wakes dominate. Downstream, the internal boundary layer thickens ($\delta_{\mathrm{IBL}} \propto x^{0.72\text{–}0.78}$) and the shear length scale grows from 0.30 m to ~ 8.6 m, with an apparent plateau near $x/h \approx 50$. Under a C2-light disclosure, this far-wake leveling represents a physical trend observed under the present grid resolution that warrants future

confirmation by mesh-independent adaptive studies. The results provide a rigorous neutral hydrodynamic baseline for vegetative roughness transitions and surface drag formulations.

Keywords: Canopy-clearing transitions; Large-eddy simulation; Internal boundary layer; Turbulent momentum budget; Shear length scale; Vegetation-atmosphere interaction; Roughness transition; Momentum budget closure; Shear layer relaxation

Article Highlights

- High-resolution simulation of wind over a forest edge matches measured canopy winds and turbulence.
- Including the smallest-scale stress term closes the momentum budget away from the edge.
- A forest edge shelters the clearing for many tree heights, guiding where models smooth the roughness.

1 Introduction

Atmospheric boundary layer flow across sharp vegetative discontinuities governs local momentum exchange, surface microclimates, and turbulent transport at forest edges Cheng et al. (2021); Venkatraman et al. (2023); de Arellano et al. (2023). When wind encounters an abrupt transition from a dense canopy to an open clearing, the sudden removal of aerodynamic drag generates streamline curvature, localized pressure gradients, and downstream wake turbulence Dupont and Brunet (2009); Dupont et al. (2008). These edge dynamics affect forest microclimates, carbon and water vapor fluxes, and windthrow vulnerability Bannister et al. (2022); Dupont et al. (2018).

Predicting flow adjustment across vegetative edges remains difficult with conventional Reynolds-Averaged Navier-Stokes (RANS) methods. Standard eddy-viscosity closures assume isotropic turbulence and local equilibrium, underpredicting anisotropic Reynolds stresses and streamline separation behind the vegetative step Li et al. (2020); Schmitt et al. (2023); Cassiani et al. (2008). Large-Eddy Simulation (LES) addresses these limitations by resolving three-dimensional energy-containing eddies, directly capturing the Kelvin-Helmholtz billows and coherent vortices that form at the canopy-clearing interface Belcher et al. (2012); Shaw and Schumann (1992); Watanabe (2004).

Experimental and numerical studies have described several features of canopy edge flows Poëtte et al. (2017); Brunet (2020); Sharma and García-Mayoral (2019); Raupach and Finnigan (1995); Finnigan (2000); Finnigan et al. (2020). Wind tunnel measurements by Markfort et al. (2014) provided detailed Particle Image Velocimetry (PIV) and Hot-Wire Anemometry (HWA) data for an idealized forest-clearing transition. While previous simulations have examined general edge effects Cassiani et al. (2008); Detto et al. (2008); Auvinen et al. (2020), few studies have evaluated the term-by-term spatial momentum budget across the transition, the balance between pressure forces

and turbulent shear fluxes, or the downstream scaling of the shear length scale L_s for the canopy-to-clearing direction. In contrast to the clearing-to-forest direction examined by dos Reis Pinheiro et al. (2024), the present work addresses the reverse canopy-to-clearing transition, for which the term-by-term momentum budget and the downstream scaling of L_s remain unexplored. These edge flows modulate ventilation, pollutant fate, and surface-energy exchange in the sheltered zone behind the edge Markfort et al. (2014); Queck et al. (2016); Dupont et al. (2010a), and they shape forest-fragmentation microclimates and the wind resource over forested terrain. Because the experimental benchmark of Markfort et al. (2014) provides aerodynamic data (velocity and Reynolds stresses), the LES is formulated under neutral, isothermal conditions to establish the resolved mechanical baseline that underpins turbulent momentum diffusivity $K_m(x,z) = -\overline{u'w'}/(\partial\overline{u}/\partial z)$ and scalar diffusivity $K_c(x,z) = K_m/Sc_t$; diagnosing K_m, K_c and $Sc_t(x,z)$ for real canopies is deferred to future scalar-dispersion work. Quantifying this hydrodynamic adjustment is a prerequisite for determining pollutant flushing time scales and for sub-grid drag and effective-roughness parameterizations in mesoscale models such as BRAMS and WRF Bohrer et al. (2009). The neutral fetch dependence reported here is the baseline. In stable air the internal boundary layer is thinner and slower to equilibrate, which suppresses vertical ventilation; in unstable air convective mixing is stronger and the recovery fetch shortens Savelyev and Taylor (2005).

Here, we simulate the wind tunnel canopy-to-clearing transition of Markfort et al. (2014) using LES with the Localised Dynamic Kinetic (LDK) sub-grid scale model Kim and Menon (1997). The dynamic formulation adjusts locally to strong shear without requiring empirical damping near walls or canopy interfaces. The objectives are: (i) to validate the LES against wind tunnel PIV and HWA measurements; (ii) to compute the spatial two-dimensional momentum budget at sub-canopy height ($z/h = 0.2$); (iii) to track the downstream evolution of the shear length scale $L_s(x)$, extending the scaling analysis previously reported for the reverse transition dos Reis Pinheiro et al. (2024) to the canopy-to-clearing configuration; (iv) to characterize the three-dimensional coherent vortex structures responsible for momentum exchange in the clearing; and (v) to evaluate diagnostic edge ventilation scales (u_{ex} and flushing time τ_{flush}) and sub-grid parameterizations for mesoscale modeling. Relative to the reverse clearing-to-forest transition of dos Reis Pinheiro et al. (2024), which used a similar LES framework, this study reverses the roughness-step direction and adds (i) the term-by-term momentum budget at sub-canopy height, (ii) the sub-grid-closed residual diagnostic, and (iii) the canopy-to-clearing scaling of $L_s(x)$; the two studies are therefore complementary rather than overlapping.

2 Materials and Methods

2.1 Governing Equations and Sub-Grid Scale Model

The filtered incompressible Navier-Stokes equations governing the large-eddy simulation in the presence of vegetative canopy drag are expressed as:

$$\frac{\partial \overline{u}_i}{\partial x_i} = 0, \tag{1}$$

$$\frac{\partial \overline{u}_i}{\partial t} + \frac{\partial (\overline{u}_i \overline{u}_j)}{\partial x_j} = -\frac{1}{\rho}\frac{\partial \overline{p}}{\partial x_i} + \nu \frac{\partial^2 \overline{u}_i}{\partial x_j^2} - \frac{\partial \tau_{ij}}{\partial x_j} + S_{u_i}, \tag{2}$$

where $\overline{u}_i = (\overline{u}, \overline{v}, \overline{w})$ denotes the resolved velocity vector in Cartesian coordinates $x_i = (x, y, z)$ corresponding to the streamwise, spanwise, and vertical directions, respectively. $\overline{p}$ is the resolved pressure, ρ is the fluid density, ν is the kinematic molecular viscosity, and $\tau_{ij} = \overline{u_i u_j} - \overline{u}_i \overline{u}_j$ represents the sub-grid scale (SGS) stress tensor.

The aerodynamic drag exerted by the vegetative elements on the flow is parameterized through the volumetric momentum sink term S_{u_i} Finnigan (2000):

$$S_{u_i} = -C_d a |\overline{\mathbf{u}}| \overline{u}_i = -C_d a \sqrt{\overline{u}_k \overline{u}_k}\, \overline{u}_i, \tag{3}$$

where $C_d = 1.0$ is the bulk canopy drag coefficient and $a = 10\,\mathrm{m}^{-1}$ is the leaf area density (LAD), corresponding to a total Leaf Area Index $LAI = \int_0^h a\,\mathrm{d}z = 1.0$ for a canopy height $h = 0.10\,\mathrm{m}$, consistent with the wind-tunnel setup of Markfort et al. (2014).

The SGS stress tensor τ_{ij} is modeled using the Localised Dynamic Kinetic (LDK) sub-grid energy formulation Kim and Menon (1997), which solves a transport equation for the sub-grid turbulent kinetic energy $k_{\mathrm{sgs}} = \frac{1}{2}(\overline{u_k u_k} - \overline{u}_k \overline{u}_k)$:

$$\frac{\partial k_{\mathrm{sgs}}}{\partial t} + \overline{u}_i \frac{\partial k_{\mathrm{sgs}}}{\partial x_i} = -\tau_{ij}\frac{\partial \overline{u}_i}{\partial x_j} - C_\varepsilon \frac{k_{\mathrm{sgs}}^{3/2}}{\Delta_f} + \frac{\partial}{\partial x_i}\left(\nu_t \frac{\partial k_{\mathrm{sgs}}}{\partial x_i}\right) + S_{k_{\mathrm{sgs}}}, \tag{4}$$

where $\Delta_f = (\Delta x \Delta y \Delta z)^{1/3}$ is the grid filter width, and the canopy-induced SGS dissipation source term is given by Kanani-Sühring and Raasch (2015); Watanabe et al. (2020); Shaw and Schumann (1992):

$$S_{k_{\mathrm{sgs}}} = -2 C_d a \sqrt{\overline{u}_k \overline{u}_k}\, k_{\mathrm{sgs}}. \tag{5}$$

The SGS stress tensor is then closed via the Boussinesq eddy-viscosity hypothesis:

$$\tau_{ij} - \frac{2}{3} k_{\mathrm{sgs}} \delta_{ij} = -2\nu_t \overline{S}_{ij} = -2 C_k k_{\mathrm{sgs}}^{1/2} \Delta_f \overline{S}_{ij}, \tag{6}$$

where $\overline{S}_{ij} = \frac{1}{2}(\partial \overline{u}_i/\partial x_j + \partial \overline{u}_j/\partial x_i)$ is the resolved strain-rate tensor, and the dynamic coefficients C_k and C_ε are determined locally using the Germano identity without

requiring global planar averaging or arbitrary clipping Basu and Porté-Agel (2006); Wurps et al. (2020).

2.2 Experimental Benchmark Dataset

The numerical simulations are validated against the experimental wind-tunnel dataset of Markfort et al. (2014), which modeled an abrupt canopy-to-clearing transition (canopy backward-facing step). In that experiment, a dense array of cylindrical roughness elements of height $h = 0.10\,\mathrm{m}$ simulated a forest canopy transitioning abruptly into a smooth clearing.

The experimental campaign utilized complementary measurement techniques:

1. **Particle Image Velocimetry (PIV):** High-resolution planar PIV was deployed in the canopy and near-wake regions ($x/h = -5$ to $x/h = 4$) with stacked Fields of View ($14\,\mathrm{cm} \times 14\,\mathrm{cm}$), providing two-dimensional instantaneous velocity vectors and Reynolds stresses up to $z/h \approx 2$.
2. **Hot-Wire Anemometry (HWA):** Crossed hot-wire probes (x-wire) sampled the far-wake boundary layer adjustment across 16 downstream stations from $x/h = -5$ to $x/h = 50$ up to vertical heights of $z/h = 8$. The smooth-wall equilibrium reference profile ($x/h \to \infty$, canopy removed; Fig. 18 of Markfort et al. (2014)) is used to assess far-wake relaxation toward equilibrium.

Table 1 summarizes the aerodynamic parameters of the experimental canopy model.

Table 1: Aerodynamic characteristics of the wind-tunnel canopy model Markfort et al. (2014).

Parameter	Symbol	Value
Canopy height	h	$0.10\,\mathrm{m}$
Leaf Area Index	LAI_{exp}	1.0
Normalized friction velocity	u_*/U_h	0.38
Zero-plane displacement height	d/h	0.70
Aerodynamic roughness length	z_0/h	0.12
Canopy drag coefficient	C_d	1.0

2.3 Computational Domain and Mesh Topology

The computational domain was configured to replicate the wind-tunnel test section, spanning $L_x \times L_y \times L_z = 150h \times 17h \times 17h$ in the streamwise, spanwise, and vertical directions, respectively (Figure 1).

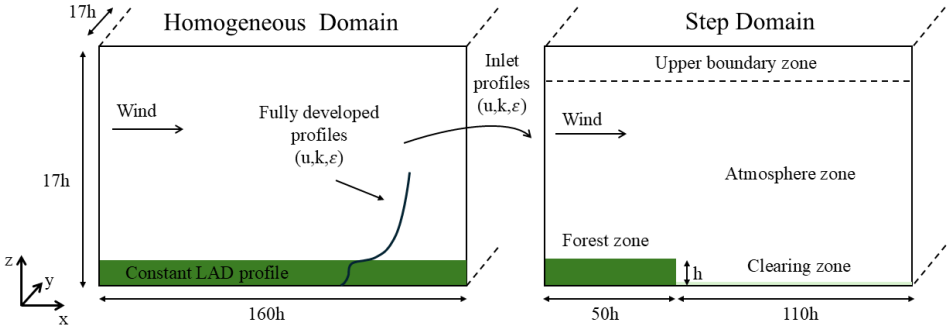


Fig. 1: Schematic representation of the computational domain: (left) homogeneous canopy domain for inflow generation; (right) backward-facing step domain modeling the canopy-to-clearing transition.

The structured grid contains 1,430,590 nodes ($N_x \times N_y \times N_z = 191 \times 70 \times 107$) and 1,389,660 hexahedral elements. The spanwise domain width of $L_y = 17h$ is sufficient to accommodate multiple energetic coherent structures across the span, ensuring that spanwise two-point velocity correlations decay toward zero within $L_y/2$ and eliminating spurious periodic confinement. Cells cluster near the canopy edge ($x/h \leq 10$) and near the ground (Figure 2). Ten cells span the canopy depth ($z \leq h$). The first wall cell height is $\Delta z_1 = 0.005h = 5 \times 10^{-4}\,\mathrm{m}$, giving a wall-normal coordinate $z^+ = \Delta z_1 u_*/\nu \approx 2.7$ based on the clearing wall friction velocity ($u_* \approx 0.082\,\mathrm{m\,s^{-1}}$; Table 2), which places the centroid well within the viscous sublayer and confirms compatibility with standard wall functions. This value corresponds to the smooth clearing roughness $z_0 = 0.03\,\mathrm{mm}$ ($z_0/h = 3 \times 10^{-4}$; Table 2), distinct from the upstream canopy roughness $z_0/h = 0.12$ in Table 1. Expansion ratios remain below 1.15 in all directions.

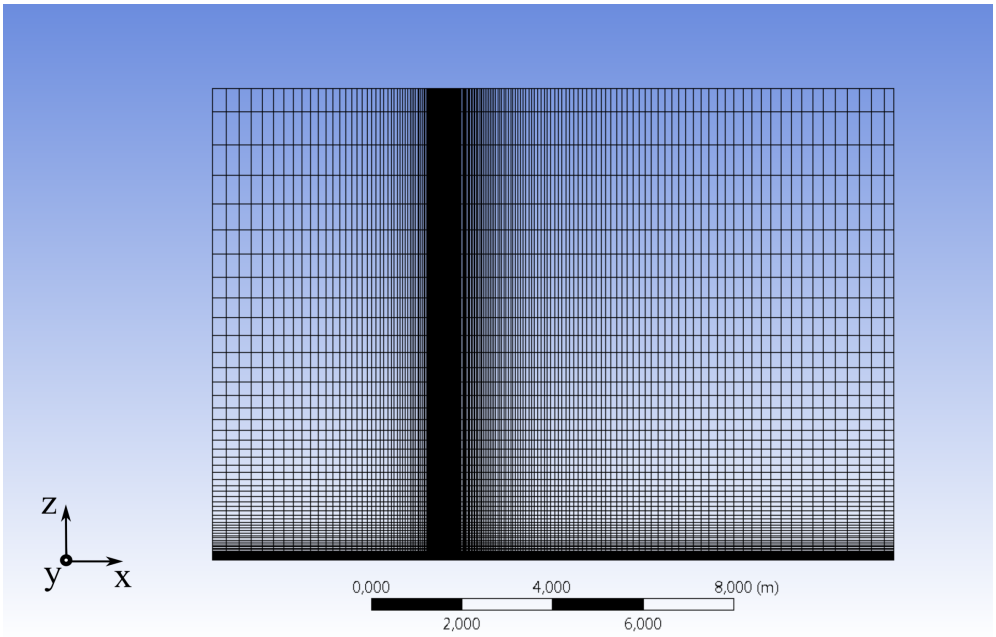


Fig. 2: Cross-sectional view of the computational mesh in the x–z plane (scale reduced for illustration), highlighting mesh refinement concentrated at the canopy interface and clearing ground.

2.4 Boundary Conditions and Numerical Scheme

Boundary conditions are prescribed as follows:

- **Inlet:** A fully developed equilibrium boundary-layer mean profile, generated via a precursor RANS simulation over a homogeneous canopy domain, is imposed at $x/h = -15$; turbulent fluctuations are superimposed at the inlet using the vortex method Mathey et al. (2006); Dalpé and Masson (2009); Cassiani et al. (2008). The distance of $10h$ between the inlet plane ($x/h = -15$) and the first measurement validation station ($x/h = -5$) corresponds to $5L_c$, where $L_c = 2/(C_d a) = 2h$ is the analytical canopy adjustment length scale Belcher et al. (2003). Because spatial adaptation of synthetic vortices into physically correlated Reynolds stresses requires 3–4L_c Bechmann and Sørensen (2010); Wurps et al. (2020), this fetch ensures that synthetic fluctuations have fully converted into realistic, divergence-free turbulence before reaching the validation field of view.
- **Outlet:** A convective outflow boundary condition with zero diffusion flux is specified at $x/h = 135$ Patankar (1980).
- **Lateral boundaries:** Periodic boundary conditions are applied in the spanwise direction (y) to simulate an infinitely wide forest edge.
- **Top boundary:** A symmetry (zero normal gradient and zero vertical velocity) condition is applied at $z/h = 17$ to prevent artificial blockage and wave reflection.

- **Bottom wall:** A standard no-slip wall condition with rough-to-smooth surface transition functions is prescribed along the canopy floor and clearing surface.

The finite-volume method in ANSYS Fluent advances the solution. SIMPLEC couples pressure and velocity. Convective momentum uses second-order central differencing. Time integration uses a second-order Non-Iterative Time Advancement (NITA) scheme with $\Delta t = 0.01\,\mathrm{s}$ (CFL < 0.8). Statistics are collected after 10 flow-through times, over $t = 5000\,\mathrm{s}$ ($> 50\,h/U_h$), long enough for second-order moments to reach stationarity.

3 Results and Discussion

3.1 Inlet Profile Validation from Precursor Simulation

Figure 3 illustrates the normalized streamwise velocity profile obtained from the precursor canopy simulation compared against the experimental inflow data.

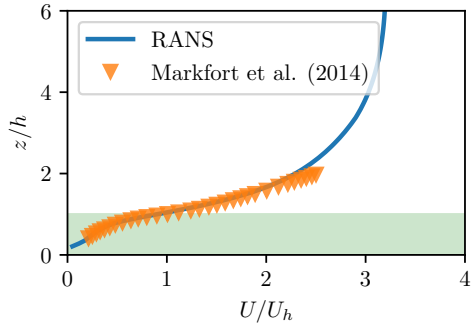


Fig. 3: Normalized streamwise velocity profile from the precursor simulation (solid line) compared with experimental inflow measurements (symbols).

The precursor simulation successfully reproduces the characteristic S-shaped inflectional velocity profile within the canopy and the logarithmic boundary layer above, providing the mean inflow field for the step-transition domain, with turbulent fluctuations superimposed via the vortex method Mathey et al. (2006); Cassiani et al. (2008); Bechmann and Sørensen (2010).

3.2 Mean Velocity Profiles and Turbulence Statistics

Figure 4 presents vertical profiles of mean velocity and turbulent statistics compared with the benchmark PIV and HWA measurements of Markfort et al. (2014). Profiles within the canopy are non-dimensionalized by the canopy-top velocity U_h and friction velocity u_*, while clearing profiles are normalized by the free-stream velocity U_0 (Table 2).

Figures 4a and 4b compare the mean streamwise velocity profiles ($\overline{u}$) across the canopy and clearing. At $x/h = -5$ inside the canopy (Figure 4a), the normalized mean

Table 2: Reference flow parameters from the experimental benchmark Markfort et al. (2014).

Parameter	Symbol	Value	Unit
Free-stream velocity	U_0	2.0	$\mathrm{m\,s^{-1}}$
Clearing aerodynamic roughness	z_0	0.03	mm
Canopy friction velocity	u_*	0.082	$\mathrm{m\,s^{-1}}$
Canopy-top velocity ratio	u_*/U_h	0.38	–

velocity $\overline{u}/U_h$ agrees closely with the field-of-view PIV measurements throughout the sub-canopy layer ($z/h < 1$). The analytical canopy adjustment scale $L_c = 2/(C_d a) = 2h$ indicates that the upstream flow reaches equilibrium before encountering the edge Belcher et al. (2003). Above the canopy ($z/h > 1$), the LES reproduces the inflectional shear layer that merges with the outer boundary layer.

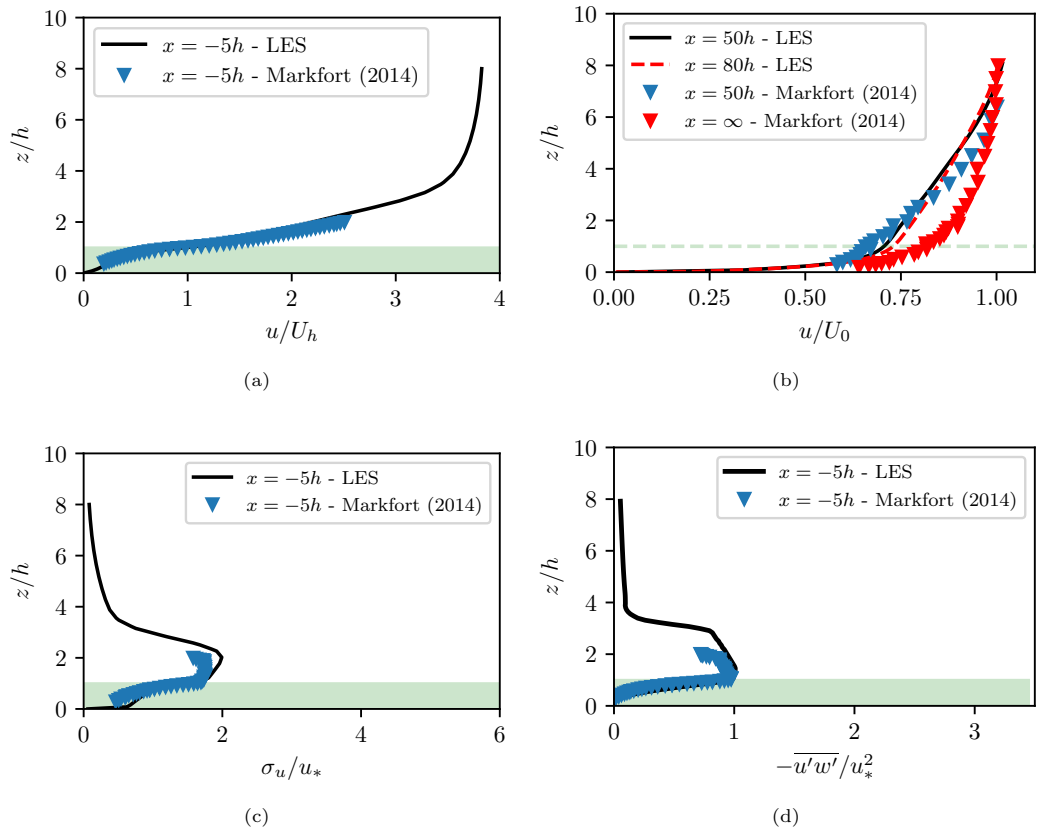


Fig. 4: Comparison of LES results with wind tunnel FoV and HWA data (Markfort et al. (2014)) for mean velocity and turbulence statistics: (a) Vertical profile of the mean streamwise velocity ($\overline{u}/U_h$) inside the canopy at $x/h = -5$ (FoV data); (b) Vertical profile of the mean streamwise velocity ($\overline{u}/U_0$) over the clearing at $x/h = 50$ (HWA data) and $x/h = 80$ (LES) versus the smooth-wall equilibrium reference ($x/h \to \infty$), showing flow adjustment; (c) Vertical profile of the longitudinal velocity standard deviation (σ_u/u_*) inside the canopy at $x/h = -5$ (FoV data); (d) Vertical profile of the Reynolds shear stress ($\overline{u'w'}/u_*^2$) inside the canopy at $x/h = -5$ (FoV data).

Figure 4b shows the downstream flow adjustment across the clearing normalized by the free-stream velocity U_0. At $x/h = 50$, the LES over-predicts velocity recovery in the region $1 < z/h < 4$ relative to the HWA data (RMSE 0.043, MAE 0.034 at $50h$; Table 3), and at $x/h = 80$ the profile lies above the smooth-wall equilibrium reference ($x/h \to \infty$) of Markfort et al. (2014) by RMSE 0.104 over $0.1 < z/h < 8$. This indicates a faster IBL recovery in the LES than observed, consistent with the coarser far-wake resolution and the continuous-drag coherence discussed below. The

IBL nonetheless thickens and converges toward the equilibrium shape Li and Liu (2021); dos Reis Pinheiro et al. (2024).

Figure 4c shows the normalized streamwise turbulence intensity $\sigma_u/u_* = \sqrt{\overline{u'^2}}/u_*$ at $x/h = -5$, a measure of the turbulence generated by the roughness jump. PIV and LES both peak at the canopy top ($z/h = 1$), where inflectional shear generates kinetic energy. Above the canopy ($z/h > 1$) the LES systematically exceeds the measurements (RMSE 0.173, MAE 0.143; Table 3), not a marginal offset.

The Reynolds shear stress $\overline{u'w'}/u_*^2$ (Figure 4d) agrees with the tunnel data inside the canopy ($z/h < 1$), where drag extracts energy, but it over-predicts the peak just above the crest ($z/h \approx 1$–1.5) by 30–40% locally (RMSE $0.395\,u_*^2$, MAE $0.315\,u_*^2$; Table 3). As discussed in LES and DNS studies of heterogeneous canopies Sützl et al. (2021); Blunn et al. (2021); Basu and Porté-Agel (2006), this bias arises from using a continuous porous drag model rather than discrete physical cylinders. In physical canopies, stem wakes generate fine-scale vortex shedding and local dissipation that accelerate the energy cascade Lopes et al. (2021); Shaw and Patton (2003). The continuous drag model homogenizes obstacle interactions across grid cells, allowing Kelvin-Helmholtz billows to retain higher coherence above the canopy Arthur et al. (2019); Dupont et al. (2010b). The vertical velocity fluctuations remain resolved across 3.6 to 4 grid cells, satisfying the resolution guideline of Wurps et al. (2020), but this does not remove the homogenization bias above h.

Table 3 quantifies the agreement between the LES and the wind-tunnel profiles of Figure 4 in terms of RMSE and MAE, computed over the overlapping normalized-height ranges after linear interpolation of the LES onto the experimental digitized points.

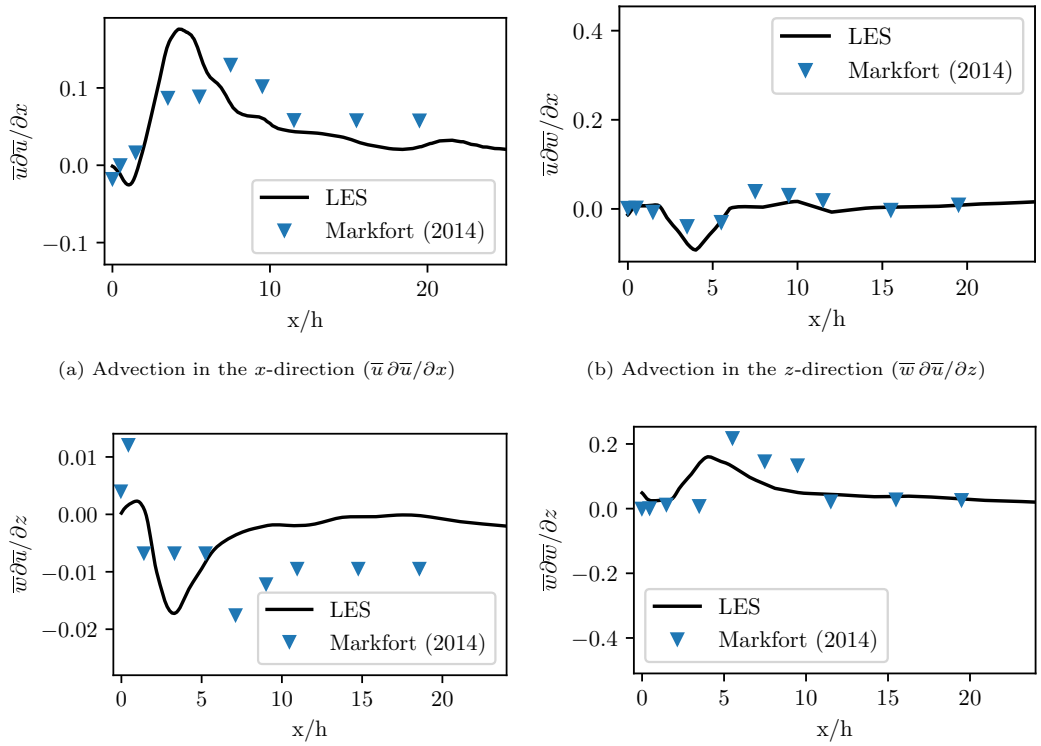
Table 3: Validation statistics (RMSE, MAE) of the LES profiles against the wind-tunnel data of Markfort et al. (2014) for the panels of Figure 4. Metrics are computed over the overlapping normalized-height range z/h (the PIV/FoV data of the $-5h$ station span the canopy layer up to $z/h \approx 2$); the LES profile is linearly interpolated onto the experimental digitized points. The Reynolds stress is expressed in the experimental normalization u_*^2 (LES u_* from the precursor, $u_*^2 = 0.0208$ m^2 s^{-2}).

Quantity, location	N	z/h range	RMSE	MAE
Mean velocity $\overline{u}/U_h$, $x/h = -5$ (FoV)	51	0.3–2.0	0.141	0.104
Mean velocity $\overline{u}/U_0$, $x/h = 50$ (HWA)	25	0.1–6.4	0.043	0.034
Mean velocity $\overline{u}/U_0$, $x/h = 80$ vs. equilibrium ref.	35	0.1–8.0	0.104	0.094
Std. dev. σ_u/u_*, $x/h = -5$ (FoV)	43	0.3–2.0	0.173	0.143
Reynolds stress $-\overline{u'w'}/u_*^2$, $x/h = -5$ (FoV)	48	0.3–2.0	0.395	0.315

These shear-layer differences above the canopy top do not dominate the sub-canopy momentum dynamics ($z/h = 0.2$) once SGS stresses are included, where the budget residual falls to $|R_x| < 0.03$ for $x/h \gtrsim 10$ (Sect. Momentum Balance Closure); within $x/h < 5$ the residual remains dispersive-dominated irrespective of the above-canopy bias dos Reis Pinheiro et al. (2024); Sützl et al. (2021).

3.3 Horizontal Profiles of the Terms of the Turbulent Momentum Equation

Figure 5 displays the longitudinal distribution of the resolved advective terms of the momentum equation at sub-canopy height $z/h = 0.2$, from the canopy edge ($x/h = 0$) to $x/h = 25$ in the clearing. The sub-canopy height $z/h = 0.2$ was selected for the detailed term-by-term budget because it coincides with the sub-canopy jet station instrumented in the experimental campaign of Markfort et al. (2014), capturing the accelerated exit flow and the localized cavity depressurization; at the canopy crest ($z/h = 1.0$), the budget is conversely dominated by shear production and strong vertical turbulent transport. All terms are non-dimensionalized by canopy height h and friction velocity u_* (Table 2). The four terms examined are $\overline{u}\,\partial\overline{u}/\partial x$ (Figure 5a), $\overline{w}\,\partial\overline{u}/\partial z$ (Figure 5b), $\overline{u}\,\partial\overline{w}/\partial x$ (Figure 5c), and $\overline{w}\,\partial\overline{w}/\partial z$ (Figure 5d).



(a) Advection in the x-direction ($\overline{u}\,\partial\overline{u}/\partial x$)

(b) Advection in the z-direction ($\overline{w}\,\partial\overline{u}/\partial z$)

(c) Advection in the x-direction ($\overline{u}\,\partial\overline{w}/\partial x$)

(d) Advection in the z-direction ($\overline{w}\,\partial\overline{w}/\partial z$)

Fig. 5: Spatial distribution of the resolved advective terms of the momentum equation at $z/h = 0.2$. Left-hand panels: terms contributing to the x-momentum equation; right-hand panels: terms contributing to the z-momentum equation. All terms are normalised by h/u_*^2.

In Figure 5a the longitudinal advection $\overline{u}\,\partial\overline{u}/\partial x$ is strongly negative just downstream of the edge ($x/h < 5$) and recovers toward zero across the clearing. The vertical advection $\overline{w}\,\partial\overline{u}/\partial z$ (Figure 5b) shows a concurrent minimum near the edge. Both change quickly because the drag $f_D = \rho C_d a|\overline{u}|\overline{u}$ vanishes at $x = 0$, so sub-canopy air accelerates into the clearing ($\partial\overline{u}/\partial x > 0$) Belcher et al. (2003); Sützl et al. (2021).

In the vertical momentum equation the two terms $\overline{u}\,\partial\overline{w}/\partial x$ and $\overline{w}\,\partial\overline{w}/\partial z$ (Figures 5c and 5d) also vary within $x/h < 10$. The first stays negative and stabilizes beyond $x/h \approx 10$; the second peaks near $x/h \approx 6$ and then decays. The pattern reflects streamline curvature as fluid above the canopy turns downward ($\overline{w} < 0$) into the clearing, consistent with deflection theory Belcher et al. (2003); Ma et al. (2020). LES peaks are slightly sharper due to local resolution at the step, but the extent and sign reversals match the tunnel.

3.3.1 Pressure-Gradient Terms

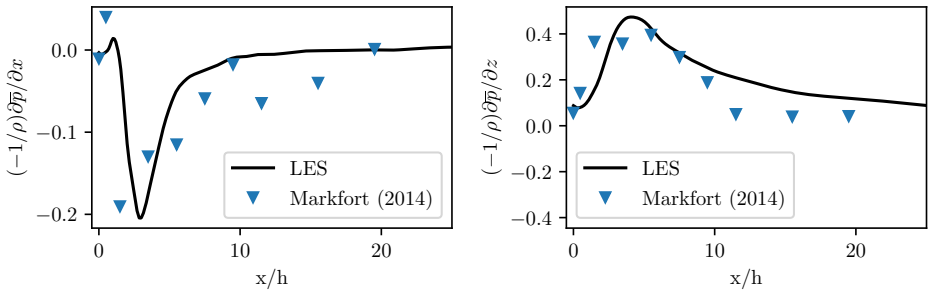
The pressure-gradient terms in the streamwise $-\frac{1}{\rho}\frac{\partial\langle\overline{p}\rangle}{\partial x}$ and vertical $-\frac{1}{\rho}\frac{\partial\langle\overline{p}\rangle}{\partial z}$ directions were evaluated in the wind tunnel experiment of Markfort et al. (2014) as residuals of the double-averaged momentum equations based on measured velocity and Reynolds stress gradients. Following double-averaging methodology Blunn et al. (2021); Sützl et al. (2021), variables represent temporal averaging $\overline{\phi}$ followed by spanwise spatial averaging $\langle\phi\rangle$. The LES evaluates the same budget consistently from its resolved fields.

Assuming statistically stationary, two-dimensional mean flow and neglecting for brevity the SGS and dispersive contributions in the printed form (they are retained in the residual analysis of Sect. Momentum Balance Closure), the non-dimensional momentum balance yields the pressure gradients as:

$$-\frac{1}{\rho}\frac{\partial\langle\overline{p}\rangle}{\partial x} = \langle\overline{u}\rangle\frac{\partial\langle\overline{u}\rangle}{\partial x} + \langle\overline{w}\rangle\frac{\partial\langle\overline{u}\rangle}{\partial z} - \frac{\partial\langle\overline{u'w'}\rangle}{\partial z} - \frac{\partial\langle\overline{u'u'}\rangle}{\partial x} - \frac{\partial\langle\tau_{xz}^{\mathrm{SGS}}\rangle}{\partial z} - \frac{\partial\langle\tau_{xx}^{\mathrm{SGS}}\rangle}{\partial x} - \frac{\partial\langle\tilde{u}\tilde{w}\rangle}{\partial z} + \ldots, \tag{7}$$

$$-\frac{1}{\rho}\frac{\partial\langle\overline{p}\rangle}{\partial z} = \langle\overline{u}\rangle\frac{\partial\langle\overline{w}\rangle}{\partial x} + \langle\overline{w}\rangle\frac{\partial\langle\overline{w}\rangle}{\partial z} - \frac{\partial\langle\overline{w'w'}\rangle}{\partial z} - \frac{\partial\langle\overline{u'w'}\rangle}{\partial x} - \frac{\partial\langle\tau_{zz}^{\mathrm{SGS}}\rangle}{\partial z} - \frac{\partial\langle\tau_{xz}^{\mathrm{SGS}}\rangle}{\partial x} - \frac{\partial\langle\tilde{w}\tilde{w}\rangle}{\partial z} + \ldots. \tag{8}$$

In the PIV-derived product, SGS and dispersive terms are unresolved and therefore implicitly absorbed in the inferred pressure gradient. Spatial differentiation of discrete PIV data further propagates measurement noise into the derived pressure gradients (gradient uncertainty scales with $\sigma_u/\Delta x$); these data therefore provide a reference for the magnitude and sign of pressure forces rather than a pointwise validation standard.



(a) Streamwise pressure gradient $(-\frac{1}{\rho}\frac{\partial \overline{p}}{\partial x})$ (b) Vertical pressure gradient $(-\frac{1}{\rho}\frac{\partial \overline{p}}{\partial z})$

Fig. 6: Horizontal distribution of the pressure-gradient terms extracted at $z/h = 0.2$. Left: streamwise direction (x); right: vertical direction (z). Normalised by h/u_*^2.

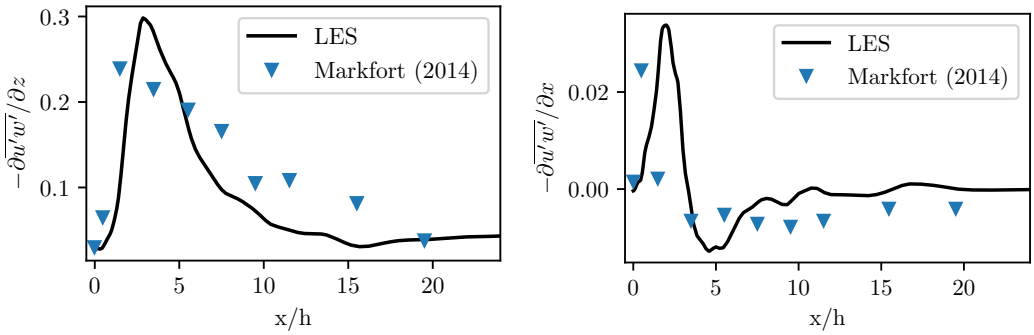
Figure 6 shows the horizontal distribution of the streamwise (a) and vertical (b) pressure-gradient terms at $z/h = 0.2$, normalized by h/u_*^2.

In the streamwise direction, $-\frac{1}{\rho}\frac{\partial \overline{p}}{\partial x}$ drops sharply behind the edge ($x/h \approx 1$–3) before decaying toward zero. This favorable pressure gradient ($\partial\overline{p}/\partial x < 0$) drives the exit-flow acceleration in the near clearing. As shown by Belcher et al. (2003); Ma et al. (2020), removing canopy form drag produces a localized low-pressure zone behind the step that accelerates sub-canopy fluid into the clearing before ground shear redevelops.

In the vertical direction, $-\frac{1}{\rho}\frac{\partial \overline{p}}{\partial z}$ shows a positive peak near the edge and then decays. This downward force deflects fluid into the clearing. Field and numerical studies report the same mechanism, with clearing edges setting vertical pressure gradients that control sub-canopy ventilation Queck et al. (2016); Dupont et al. (2010a). The LES reproduces the peak locations and the downstream decay within the uncertainty of the PIV-derived pressure.

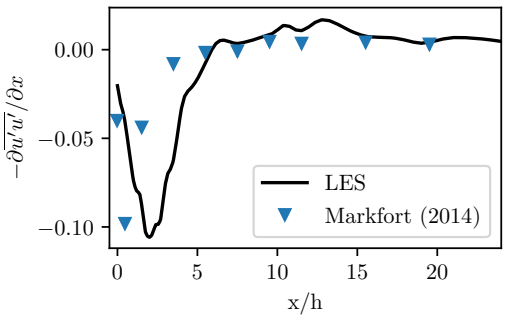
3.3.2 Reynolds-Stress Divergence Terms

Figure 7 shows the divergence terms of the Reynolds stress tensor along the x-axis at $z/h = 0.5$, normalized by h/u_*^2. We evaluate the shear-stress divergence terms $-\frac{\partial \overline{u'w'}}{\partial z}$ (Figure 7a) and $-\frac{\partial \overline{u'w'}}{\partial x}$ (Figure 7b), and the normal-stress divergence terms $-\frac{\partial \overline{u'^2}}{\partial x}$ (Figure 7c) and $-\frac{\partial \overline{w'^2}}{\partial z}$ (Figure 7d).

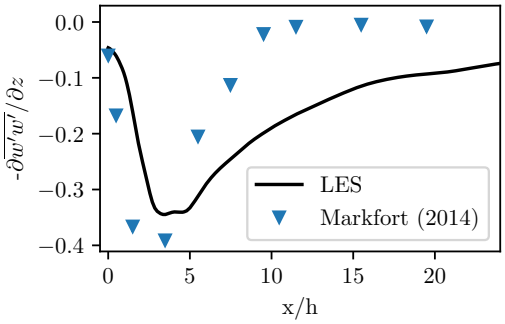


(a) Shear stress divergence in x ($-\partial\overline{u'w'}/\partial z$)

(b) Shear stress divergence in z ($-\partial\overline{u'w'}/\partial x$)



(c) Normal stress divergence in x ($-\partial\overline{u'^2}/\partial x$)



(d) Normal stress divergence in z ($-\partial\overline{w'^2}/\partial z$)

Fig. 7: Distribution of the Reynolds-stress divergence terms at $z/h = 0.5$. Left-hand panels: terms contributing to the x-momentum equation; right-hand panels: terms contributing to the z-momentum equation. All terms are normalised by h/u_*^2.

The vertical shear stress divergence $-\frac{\partial\overline{u'w'}}{\partial z}$ (Figure 7a) shows a positive peak immediately downstream of the canopy edge ($x/h \approx 1$), followed by relaxation toward the clearing. Vertical turbulent momentum transport is therefore concentrated near the interface and diminishes as the mixing layer expands into the clearing. In contrast, the longitudinal shear divergence $-\frac{\partial\overline{u'w'}}{\partial x}$ (Figure 7b) is an order of magnitude smaller, indicating that longitudinal shear gradients contribute little to the vertical momentum balance at this height.

For the normal stress divergences, $-\frac{\partial\overline{u'^2}}{\partial x}$ (Figure 7c) exhibits a localized negative dip behind the edge before returning to near zero. Conversely, $-\frac{\partial\overline{w'^2}}{\partial z}$ (Figure 7d) is strongly negative near the edge and decays monotonically downstream. Vertical velocity fluctuations therefore dominate downward kinetic energy transport and balance the vertical pressure gradient induced by the step.

The peaks in $-\partial\overline{u'w'}/\partial z$ and $-\partial\overline{w'^2}/\partial z$ confirm that the edge triggers shear-layer instabilities Ma et al. (2020); Frank and Ruck (2008). Removing canopy drag shifts the

kinetic-energy budget from wake-scale dissipation to shear production at the interface, which drives the spatial divergence of the Reynolds stress tensor Blunn et al. (2021); Sützl et al. (2021).

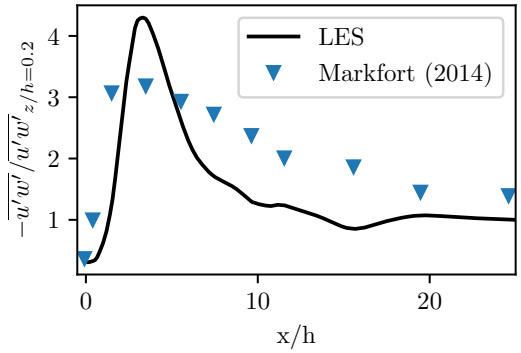


Fig. 8: Longitudinal distribution of the Reynolds shear stress $\overline{u'w'}$ normalised by the reference value measured at $x/h = 6$ and $z/h = 0.2$.

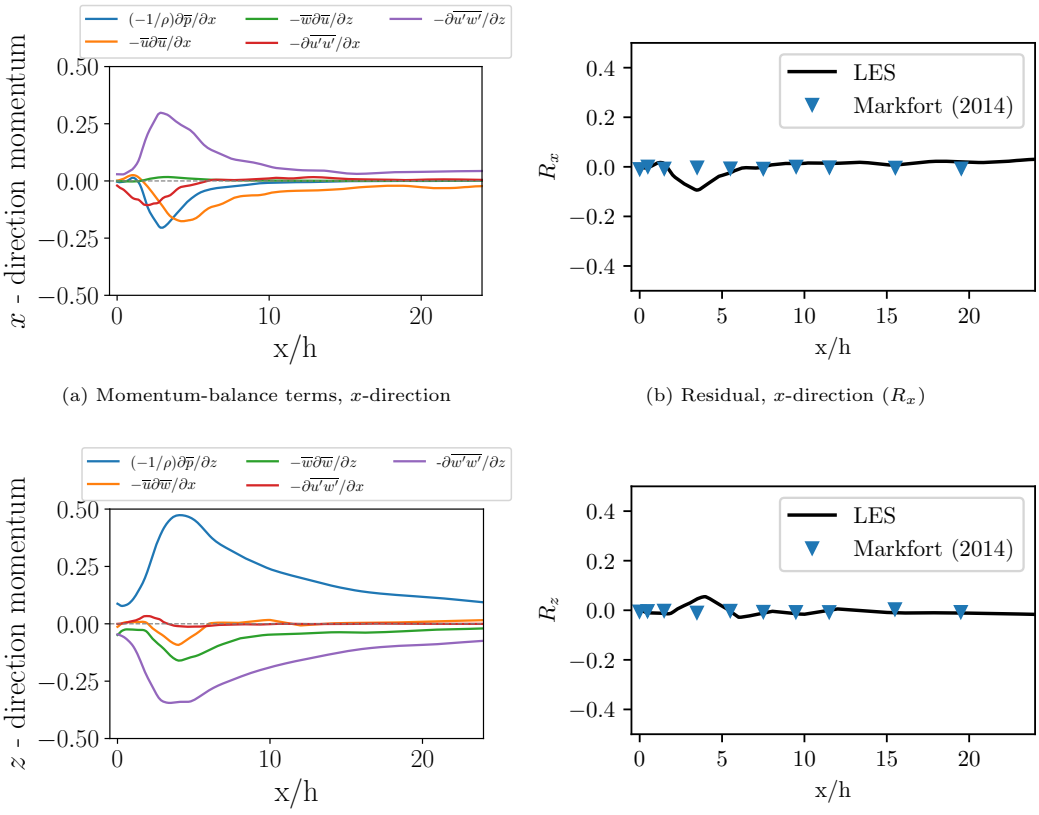
Figure 8 presents the longitudinal evolution of the Reynolds shear stress $-\overline{u'w'}$ at $z/h = 0.2$. A peak appears after the canopy edge ($x/h \approx 1$–2), showing downward momentum injection into the sub-canopy layer. Elevated shear stress persists up to $x/h \approx 10$, after which $-\overline{u'w'}$ relaxes toward the clearing state. The LES results match the wind tunnel PIV measurements in peak location, magnitude, and relaxation rate.

3.3.3 Momentum Balance Closure and Residual Analysis

Figures 9a and 9b display the terms of the double-averaged streamwise momentum equation and their residual R_x at $z/h = 0.2$. In Figure 9a, the favorable pressure gradient dominates near the edge ($x/h < 5$) and is counterbalanced primarily by advective deceleration and vertical shear-stress divergence. The residual is defined as

$$R_x = \left[\langle\overline{u}\rangle\frac{\partial\langle\overline{u}\rangle}{\partial x}+\langle\overline{w}\rangle\frac{\partial\langle\overline{u}\rangle}{\partial z}+\frac{1}{\rho}\frac{\partial\langle\overline{p}\rangle}{\partial x}-\frac{\partial\langle\tau_{xz}^{\mathrm{SGS}}\rangle}{\partial z}-\frac{\partial\langle\tau_{xx}^{\mathrm{SGS}}\rangle}{\partial x}-\frac{\partial\langle\overline{u'w'}\rangle}{\partial z}-\frac{\partial\langle\overline{u'u'}\rangle}{\partial x}+\langle S_u\rangle\right]_{z/h=0.2}, \tag{9}$$

with an analogous expression for R_z; dispersive (form-induced) stresses $\langle\tilde{u}\tilde{w}\rangle$ are not resolved by the continuous porous-medium drag and therefore appear in the residual when present.



(a) Momentum-balance terms, x-direction

(b) Residual, x-direction (R_x)

(c) Momentum-balance terms, z-direction

(d) Residual, z-direction (R_z)

Fig. 9: Distribution of the momentum-balance terms (left panels) and the resulting residuals (right panels) at $z/h = 0.2$ including the sub-grid stress divergence. Top row: x-direction; bottom row: z-direction. All quantities are normalised by h/u_*^2. The residual includes SGS and, where present, unresolved dispersive contributions.

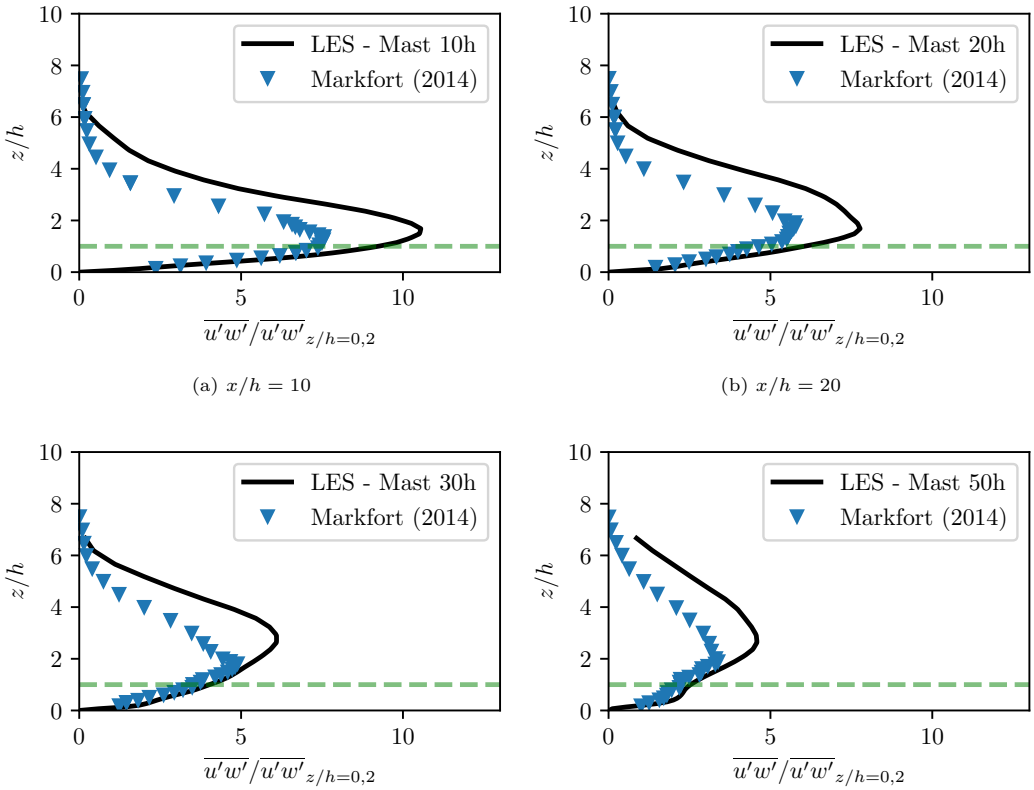
In Figure 9b, the residual R_x oscillates in the immediate transition zone ($x/h < 5$), where spatial gradients and streamline curvature are largest. This localized residual is expected and was previously misattributed to numerical error alone: flows over heterogeneous rough surfaces generate stationary dispersive momentum fluxes ($\langle\tilde{u}\tilde{w}\rangle$) and form-induced stresses that can account for 20%–50% of the momentum exchange within the obstacle sublayer Blunn et al. (2021); Sützl et al. (2021). Because the present continuous drag model does not resolve individual obstacle wakes, these dispersive stresses are absent from the resolved grid scale at the edge and remain in R_x. When the SGS divergence (Eq. 6) is included, the residual downstream of $x/h \approx 10$—where the flow transitions into a developing IBL over the smooth clearing—falls to $|R_x| < 0.03$, indicating closure of the resolved+SGS budget to within 3% of the normalizing scale.

Within $x/h < 5$ the residual remains O(0.1) and is dominated by the missing dispersive component, not by iterative convergence error.

Figures 9c and 9d show the vertical momentum budget and its residual R_z. Figure 9c demonstrates a direct balance between the vertical pressure gradient force and the normal-stress divergence $-\partial\overline{w'^2}/\partial z$, with SGS contributions an order of magnitude smaller at this height. The vertical residual R_z (Figure 9d) remains near zero across the domain ($|R_z| < 0.02$) with negligible vertical dispersive contribution, confirming vertical momentum conservation within the evaluated budget.

4 Turbulence Statistics, Wake Evolution, and Coherent Vortices

Figure 10 presents the vertical profiles of the Reynolds shear stress $\overline{u'w'}$ at four downstream stations across the clearing ($x/h = 10, 20, 30$, and 50), normalized by the reference value at $x/h = 30, z/h = 0.2$.

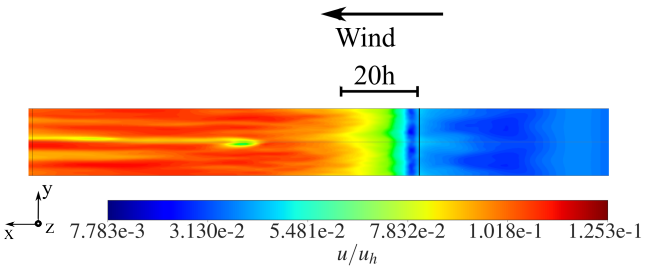


(a) $x/h = 10$ (b) $x/h = 20$

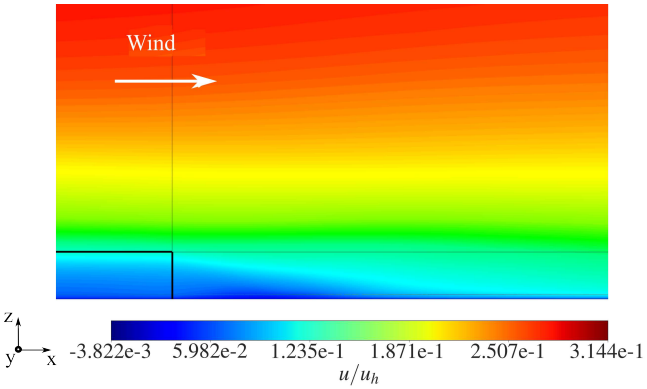
(c) $x/h = 30$ (d) $x/h = 50$

Fig. 10: Vertical profiles of the Reynolds shear stress $\overline{u'w'}$ at downstream positions (a) $10h$, (b) $20h$, (c) $30h$, and (d) $50h$. Each profile is normalised by the reference value at $x/h = 30$ and $z/h = 0.2$.

The LES captures the vertical structure and downstream attenuation of the turbulent shear stress across the clearing. In the near-surface layer ($z/h \lesssim 1$), numerical results agree with the experimental data within the scatter of the HWA profiles, reproducing the decay of canopy-induced shear up to $x/h \approx 30$. Above canopy height ($z/h \gtrsim 1$) and in the far wake ($x/h \gtrsim 30$), the LES over-predicts stress magnitude by up to a factor ~ 1.3–1.5 in the shear layer, consistent with slower SGS/numerical dissipation of large coherent structures advected from the canopy interface and with the coarser far-wake mesh (C2-light) Lopes et al. (2021); Yang et al. (2006).



(a) Top view, x–y plane at $z/h = 0.2$



(b) Side view, x–z plane

Fig. 11: Contours of the time-averaged streamwise velocity normalised by $U = 2\,\mathrm{m\,s^{-1}}$: (a) wake structure viewed from above; (b) flow transition from the canopy into the clearing.

Figure 11 displays the time-averaged velocity fields in the horizontal and vertical planes. In the horizontal plane at $z/h = 0.2$ (Figure 11a), the sub-canopy flow accelerates as it exits the canopy. In the vertical plane (Figure 11b), the exit flow exhibits strong shear at the canopy crest that diffuses downward, forming an Internal Boundary Layer (IBL) over the smooth clearing Li and Liu (2021).

The turbulent shear length scale L_s, characterizing the thickness of the mixing layer at the canopy crest (the distance over which the velocity gradient relaxes from its peak at $z = h$ Raupach and Finnigan (1995); Finnigan (2000)) and the dominant energetic eddy size of the shear layer, was evaluated at the upstream canopy reference location ($x = -5h$) and across five clearing positions ($x = 10h, 20h, 30h, 50h$, and $80h$) as:

$$L_s = \frac{\overline{u}(h)}{\frac{\partial \overline{u}}{\partial z}\big|_{z=h}}. \tag{10}$$

In the clearing region ($x/h > 0$), physical canopy elements are absent; nevertheless, evaluating Eq. (12) at the fixed elevation $z = h = 0.10\,\mathrm{m}$ (the upstream canopy top height) provides an operational diagnostic tracer of the elevated remnant shear layer

advected from the forest edge. This tracks the vertical expansion, upward diffusion, and progressive relaxation of the mixing-layer relic until its complete assimilation into the developing smooth-wall Internal Boundary Layer (IBL) Cheng et al. (2021); Li and Liu (2021).

Together with L_s, the visual thickness of the internal boundary layer $\delta_{\mathrm{IBL}}(x)$ was diagnosed from the wall-normal location where $\overline{u}(z)$ recovers to 99% of the smooth-wall equilibrium profile at the same x. Across the clearing, the diagnosed IBL thickness follows a characteristic power-law growth $\delta_{\mathrm{IBL}}/h \approx A(x/h)^p$ with an exponent $p \approx 0.72$–0.78. This scaling is in close agreement with classical rough-to-smooth boundary layer transition theory ($p \approx 0.8$; Belcher et al. (2003); Savelyev and Taylor (2005)) and corroborates the monotonic broadening of the shear layer.

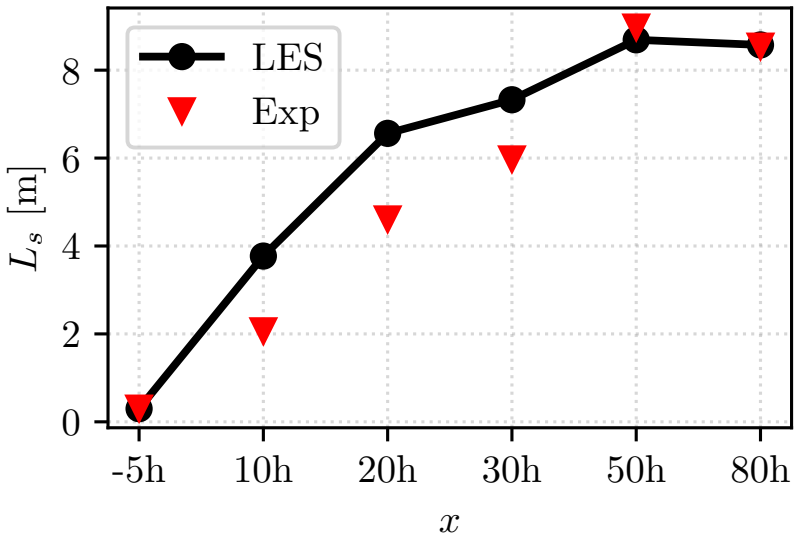
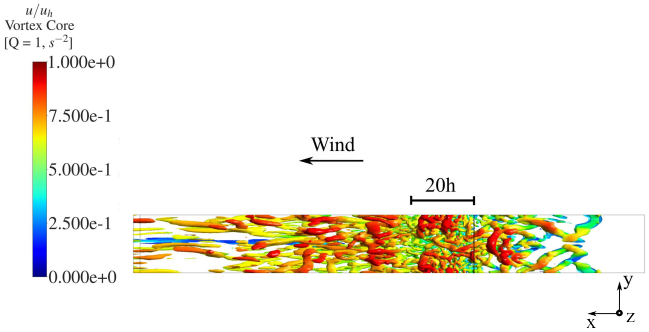


Fig. 12: Evolution of the turbulent shear length scale L_s from the upstream canopy reference ($x = -5h$) through the clearing downstream positions ($x = 10h, 20h, 30h, 50h$, and $80h$), comparing LES results with the experimental benchmark of Markfort et al. (2014); the $80h$ experimental reference corresponds to the smooth-wall equilibrium profile ($x/h \to \infty$, Fig. 18 of Markfort et al. (2014)). LES far-wake points ($x/h \geq 50$) are shown with an open symbol to flag the coarser far-wake mesh (C2-light disclosure; see Limitations).

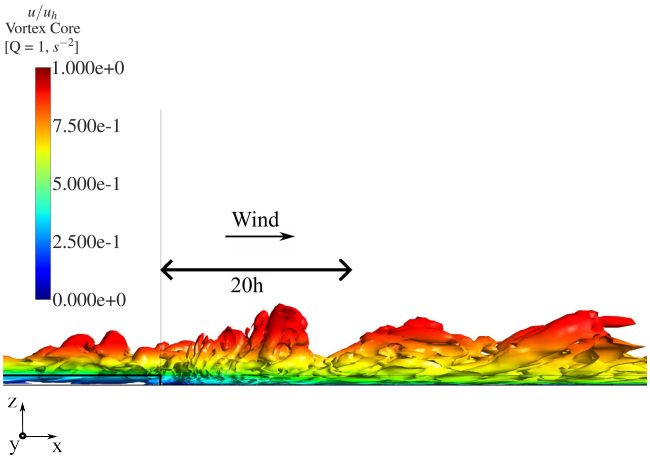
Figure 12 shows the downstream evolution of L_s across the transition. Inside the fully developed canopy at $x = -5h$, strong inflectional shear at $z = h$ produces small shear scales of $L_s \approx 0.30$ m in the LES and 0.31 m in the experimental data of Markfort et al. (2014). Downstream of the edge, sub-canopy flow acceleration weakens the vertical velocity gradient $\partial\overline{u}/\partial z$ at the crest level, causing L_s to increase monotonically across

the clearing from 3.77 m at $x = 10h$ to 8.69 m at $x = 50h$. In the far wake at $x = 80h$, the shear scale is 8.57 m, statistically indistinguishable from the $50h$ value and within 2% of the smooth-wall equilibrium reference scale ($x/h \to \infty$, Fig. 18 of Markfort et al. (2014)). Taken at face value this suggests a plateau and vertical expansion/relaxation of the shear layer into an IBL, consistent with the concurrent IBL thickening seen in Fig. 11 and with prior canopy scaling Raupach and Finnigan (1995); Belcher et al. (2003); Li and Liu (2021); dos Reis Pinheiro et al. (2024).

However, under the C2-light disclosure, this far-wake plateau coincides with the coarser streamwise/vertical resolution beyond $x/h \approx 10$ (see Limitations and Fig. 2) and must be interpreted as a physical trend observed under the present grid resolution requiring confirmation by mesh-independent studies rather than an established numerical asymptote. A power-law fit to the present clearing points yields $L_s/h \propto (x/h)^n$ with $n \approx 0.45$–0.55 between $10h$ and $50h$, before the apparent saturation; this exponent and the IBL growth are offered as a baseline for comparison with heterogeneous-canopy studies Patton and Katul (2009); Bohrer et al. (2009) and for future RANS/OpenFOAM sensitivity and AMR LES verification. The close LES–experiment agreement in the high-resolution near wake ($x/h \leq 20$), where resolution guidelines are satisfied (3.6–4 cells per vertical fluctuation; Wurps et al. (2020)), nonetheless demonstrates that the model captures the spatial adjustment of mixing scales across the canopy step transition.



(a) Aerial view



(b) Lateral view

Fig. 13: Coherent vortex structures identified using the Q-criterion ($Q = 100\ \mathrm{s}^{-2}$), viewed from aerial (a) and lateral (b) perspectives.

Instantaneous vortex structures identified via the Q-criterion ($Q = 100\,\mathrm{s}^{-2}$, Figure 13) show hairpin and horseshoe vortices shedding from the canopy edge. These vortices originate from shear instabilities at the canopy crest and advect into the clearing, enhancing vertical momentum mixing up to $x/h \approx 20$ Dupont and Brunet (2008, 2009); Detto et al. (2008); Irvine et al. (1997).

4.1 Environmental Implications: Diagnostic Edge Ventilation and Atmospheric Parameterizations

The turbulent flow adjustment across the canopy-to-clearing transition has direct consequences for environmental processes, including scalar exchange, pollutant ventilation, and the parameterization of fragmented landscapes in mesoscale meteorological models. In turbulent canopy flows, the turbulent momentum diffusivity $K_m(x, z)$ and turbulent scalar diffusivity $K_c(x, z)$ (governing passive scalars such as heat, moisture, and air

pollutants) are linked through the turbulent Schmidt number Sc_t Raupach (1987); Cassiani et al. (2008):

$$K_m(x,z) = -\frac{\overline{u'w'}}{\frac{\partial \overline{u}}{\partial z}}, \quad K_c(x,z) = \frac{K_m(x,z)}{Sc_t}. \tag{11}$$

While standard gradient-diffusion models frequently assume a constant Reynolds analogy ($Sc_t \approx 1.0$), experimental and numerical studies in vegetative roughness sublayers demonstrate that Sc_t is non-universal and typically ranges between 0.5 and 0.9 in regions dominated by coherent sweep-ejection cycles and non-equilibrium shear Tominaga and Stathopoulos (2007); Philips et al. (2013); Brunet (2020). Because the experimental wind-tunnel campaign of Markfort et al. (2014) is an aerodynamic benchmark without scalar concentration measurements, the present LES was intentionally formulated as an isothermal, neutral mechanical baseline. This isolates the hydrodynamic mechanisms driving scalar exchange without introducing uncalibrated scalar model constants. Because this work delivers the hydrodynamic baseline rather than scalar transport, the spatially variable turbulent Schmidt number $Sc_t(x,z)$, the scalar diffusivity $K_c(x,z)$ and the effective roughness $z_{0,\mathrm{eff}}(x)$ are explicitly deferred to future work (Sect. 5.1).

From the resolved Reynolds shear stress field, first-order diagnostic scales for interfacial air exchange and sheltered-zone ventilation can be directly deduced Raupach (1987); Raupach et al. (1996); Dupont and Brunet (2008); Queck et al. (2016). At the canopy crest level ($z = h$), the vertical turbulent exchange velocity $u_{\mathrm{ex}}(x)$ scales with the local friction velocity / shear stress:

$$u_{\mathrm{ex}}(x) \sim \sqrt{-\overline{u'w'}\big|_{z=h}}(x). \tag{12}$$

The characteristic residence or flushing time scale $\tau_{\mathrm{flush}}(x)$ of the sheltered sub-canopy cavity immediately behind the forest edge is then estimated as:

$$\tau_{\mathrm{flush}}(x) \approx \frac{h}{u_{\mathrm{ex}}(x)} \approx \frac{h}{\sqrt{-\overline{u'w'}\big|_{z=h}}(x)}. \tag{13}$$

Because $-\overline{u'w'}$ reaches a maximum immediately behind the edge ($x/h \approx 1$–3; Figs. 8 and 10) due to shear-layer billows and advected hairpin vortices (Fig. 13), the flushing time scale reaches a local minimum in the near wake. Under this neutral hydrodynamic baseline, the diagnostic time scale indicates vigorous initial vertical air renewal and provides the mechanical foundation for rapid scavenging of passive ground-level pollutants or forest-edge moisture into the overlying stream in subsequent scalar parameterizations. Further downstream ($x/h > 10$), as the shear stress relaxes toward the smooth-wall value, u_{ex} decreases, increasing τ_{flush} and shifting the transport regime from rapid vertical ejection to developing boundary-layer advection.

In real-world fragmented canopies, this mechanical baseline is further modulated by thermal stratification Savelyev and Taylor (2005); Jocher et al. (2020). Under unstable

daytime conditions (solar heating of the clearing), buoyant convective plumes accelerate vertical mixing, reducing τ_{flush} and shortening the transition fetch below $50h$ ($< 500\,\text{m}$ for $h = 10$–$20\,\text{m}$). Conversely, under stable nocturnal conditions, negative buoyancy dampens vertical velocity fluctuations $\overline{w'^2}$, elevating τ_{flush} and facilitating the pooling of cold air, ground-level agrochemicals, or vehicular pollutants within the sheltered zone Lin et al. (2018); Bannister et al. (2022).

Finally, these fetch-dependent dynamics provide valuable input for sub-grid drag and effective-roughness parameterizations in mesoscale atmospheric models, such as BRAMS and WRF Bohrer et al. (2009); de Arellano et al. (2023). In typical regional simulations with grid spacings of $\Delta x \approx 1$–$5\,\text{km}$, vegetative edges are entirely sub-grid. Rather than applying an abrupt step change in aerodynamic roughness length z_0 and displacement height d, the gradual adjustment of $L_s(x)$ and momentum fluxes observed between $x/h = 10$ and 50 establishes the spatial fetch (500–1000 m) required for blending schemes to transition smoothly from canopy effective parameters ($z_{0,\text{canopy}}/h \approx 0.12, d/h \approx 0.7$) to open-clearing values ($z_{0,\text{clearing}} \approx 3 \times 10^{-4} h$).

5 Conclusions

Large-eddy simulations of an abrupt canopy-to-clearing transition reproduce the primary flow features observed in wind tunnel experiments, including sub-canopy velocity profiles, turbulent stress distributions, and wake adjustment distances, and extend them with a fetch-dependent view relevant to environmental transport. The flow field divides into an edge-dominated near wake ($x/h < 20$), governed by favorable streamwise pressure gradients and coherent vortex shedding, and a far-wake recovery region where an internal boundary layer (IBL) develops over the clearing and controls the relaxation of surface fluxes.

Term-by-term momentum-budget analysis at $z/h = 0.2$ shows that resolved advection, pressure gradients and Reynolds-stress divergences peak within five canopy heights of the edge. When the sub-grid stress divergence $-\partial\tau_{ij}/\partial x_j$ is included, the residual falls to $|R_x| < 0.03$ for $x/h \gtrsim 10$; within $x/h < 5$ the residual is dominated by dispersive (form-induced) stresses $\langle\tilde{u}\tilde{w}\rangle$ from unresolved obstacle wakes (20–50% of exchange in heterogeneous canopies), which are absent in the continuous porous-medium representation at the present resolution. This closure behaviour indicates that the porous-drag LES resolves the dominant transition dynamics beyond the immediate edge zone, while pinpointing where explicit dispersive or discrete-obstacle treatments are required.

The shear length scale $L_s = \overline{u}(h)/(\partial\overline{u}/\partial z|_{z=h})$ increases from 0.30 m within the canopy ($x/h = -5$) to $\sim 8.6\,\text{m}$ for $x/h \geq 50$ and shows an apparent plateau at $x/h = 80$ (8.57 m, within 2% of the smooth-wall equilibrium reference). In the present LES, this far-wake leveling coincides with the coarser far-wake mesh ($x/h > 10$; see Limitations) and is therefore reported as a C2-light trend reflecting physical shear relaxation under the present grid resolution that awaits confirmation by mesh-independent studies (planned RANS/OpenFOAM sensitivity and future AMR LES). The concurrent thickening of the IBL ($\delta_{\text{IBL}} \propto x^{0.72\text{–}0.78}$) and weakening of $\partial\overline{u}/\partial z|_h$ nonetheless demonstrate that shear-layer relaxation and IBL development extend into the far wake, consistent with prior canopy scaling Raupach and Finnigan (1995);

Belcher et al. (2003); Li and Liu (2021) and with the reverse-transition analysis dos Reis Pinheiro et al. (2024).

If the wind-tunnel scaling is tentatively extended to field canopies with $h = 10$–$20\,\mathrm{m}$, assuming Reynolds-number independence for aerodynamically fully rough boundary layer flows ($Re_* \gg 1$) and neutral stratification, the corresponding dimensional fetches are of order 100–200 m and 500–1000 m; these are conditional estimates, as large-scale outer atmospheric turbulence and Coriolis forcing may further modulate far-wake recovery. Beyond those fetches homogeneous effective-roughness treatments ($z_{0,\mathrm{eff}}, d_{\mathrm{eff}}, u_{*,\mathrm{eff}}$) become tenable for surface exchange, deposition, and momentum fluxes in the sheltered clearing. This neutral baseline bounds the stratified cases. Unstable air shortens the fetch; stable air lengthens it and thins the internal boundary layer Savelyev and Taylor (2005). The fetch-dependent profiles can set sub-grid drag and effective roughness in mesoscale models such as BRAMS at $\Delta x \approx 1$–$5\,\mathrm{km}$ Bohrer et al. (2009), and they give shear and turbulence intensity versus distance for wind-resource assessment behind forest edges.

5.1 Limitations and Future Directions

Limitations

- A continuous porous medium with uniform leaf area density ($a = 10\,\mathrm{m}^{-1}$) and constant drag coefficient ($C_d = 1.0$) represents the canopy. This omits individual stem wakes and crown heterogeneity and homogenizes Kelvin-Helmholtz coherence above $z/h \approx 1$ (RMSE $0.395\,u_*^2$ for $\overline{u'w'}$; see Sect. Mean Velocity Profiles);
- Refinement clusters near the edge ($x/h \leq 10$), so the far clearing ($x/h > 10$) is coarser. Under this C2-light disclosure the L_s plateau for $x/h \gtrsim 50$ (Fig. 12) and the exact IBL-growth rate are reported as physical trends observed under the present grid resolution rather than proven grid-independent asymptotes. Statistics are averaged over 5000 s ($> 50\,h/U_h$) after 10 flow-through times, but formal multi-mesh studies remain a priority;
- Conditions are neutral and isothermal, without thermal stratification or diurnal cycles, matching the experimental aerodynamic dataset of Markfort et al. (2014). Stable air thins the internal boundary layer and delays equilibrium; unstable air enhances mixing and shortens the fetch Savelyev and Taylor (2005). The reported fetches are therefore the neutral baseline for pollutant, heat and moisture ventilation;
- PIV-derived pressure gradients come from discrete momentum residuals, so differentiation and sampling noise ($\propto \sigma_u/\Delta x$) propagate into ∇p. Together with unresolved SGS and dispersive stresses, this gives $\mathrm{O}(0.05$–$0.1h/u_*^2)$ pointwise uncertainty and precludes point-wise validation of ∇p (see Sect. Pressure-Gradient Terms);
- Within $x/h < 5$ dispersive (form-induced) stresses $\langle\tilde{u}\tilde{w}\rangle$ (20–50% of exchange) dominate the residual and are absent in the drag model. Closure to $|R_x| < 0.03$ holds only for $x/h \gtrsim 10$ with SGS included and only at $z/h = 0.2$.

Future Directions

- Incorporate vertically varying leaf area density profiles ($a(z)$) and dynamic drag coefficients to evaluate crown architecture effects and discrete-obstacle wake interactions;
- Extend the simulations to thermally stratified boundary layers (stable/unstable) to bracket the neutral baseline fetches reported here and assess buoyancy effects on IBL growth and pollutant trapping;
- Perform direct large-eddy simulations of passive and reactive scalar transport (heat, moisture, trace gases, and particulate matter) with spatially variable turbulent Schmidt numbers $Sc_t(x, z)$, validated against dedicated tracer-dispersion experiments (such as the TurbEfa forest-edge campaign Queck et al. (2016));
- Perform C2-light grid-sensitivity confirmation via RANS/OpenFOAM at two resolutions focused on $x/h > 10$ and, resources permitting, via AMR LES to establish mesh-independent L_s and IBL-growth exponents ($L_s/h \propto (x/h)^n$; $n \approx 0.45$–0.55 in the present data) and to benchmark heterogeneous-canopy findings Patton and Katul (2009); Bohrer et al. (2009);
- Translate fetch-dependent effective-roughness ($z_{0,\mathrm{eff}}(x), d_{\mathrm{eff}}(x), u_{*,\mathrm{eff}}(x)$) into a subgrid blending parameterization for BRAMS and WRF at $\Delta x \sim 1$–$5\,\mathrm{km}$ Bohrer et al. (2009), and evaluate wind-energy shear/TI implications downstream of forest edges.

Acknowledgements. This research was conducted under the R&D program of the University of Brasília in collaboration with Eletrobras Furnas, within the framework of the BRAMS wind-energy research program. The authors thank the funding agencies and institutions that supported this work (details in the Funding section).

Declarations

Funding

This research was conducted under R&D project PD-0394-1709/2017 funded by ANEEL and supported by Eletrobras Furnas. Additional funding was provided by ANEEL under project P&D 06899-0123/2023, the CT-ENERG Program (CNPq/MCTI 408020/2022-9), and doctoral fellowships from CAPES and CNPq.

Conflict of Interest

The authors declare that they have no financial or non-financial competing interests that are directly or indirectly related to the work submitted for publication.

Ethics Approval and Consent to Participate

Not applicable. This study does not involve human participants, animal experiments, or tissue samples.

Consent for Publication

Not applicable.

Data Availability Statement

The simulated datasets are stored in the Energy and Environmental Laboratory repository (University of Brasília). The curve data underlying the figures and the validation tables are available from the corresponding author; the large three-dimensional raw fields are released on a documented data-use request. Derived data will be deposited in an open repository (Zenodo) upon acceptance. The experimental validation benchmark data are publicly documented in Markfort et al. (2014) (PIV/HWA profiles and Fig. 18 smooth-wall reference).

Code Availability

The computational mesh generation procedures, ANSYS Fluent user-defined functions for canopy drag and the localized dynamic SGS model, and the post-processing Python scripts used to evaluate momentum balances (including SGS and residual diagnostics), shear length scale L_s and coherent-structure diagnostics are available from the corresponding author upon reasonable request and will be archived with the derived-data DOI upon acceptance. A minimal OpenFOAM RANS sensitivity case for the far-wake grid study is in preparation and will be shared with the archived release.

Author Contributions (CRediT)

Luis Aramis R. Pinheiro: Conceptualization, Methodology, Software, Formal analysis, Investigation, Data curation, Visualization, Writing – original draft. **Rafael C. F. Mendes**: Methodology, Software, Validation, Visualization, Writing – review and editing. **Mário B. de Siqueira**: Conceptualization, Methodology, Supervision, Formal analysis, Investigation, Writing – review and editing. **Antonio C. P. Brasil Jr**: Funding acquisition, Project administration, Resources, Supervision, Writing – review and editing. All authors read and approved the final manuscript and agree to be accountable for all aspects of the work.

References

de Arellano JV, Hartogensis O, Benedict I, et al (2023) Advancing understanding of land–atmosphere interactions by breaking discipline and scale barriers. Annals of the New York Academy of Sciences 1522:74 – 97. https://doi.org/10.1111/nyas.14956

Arthur RS, Mirocha JD, Lundquist KA, et al (2019) Using a canopy model framework to improve large-eddy simulations of the neutral atmospheric boundary layer in the weather research and forecasting model. Monthly Weather Review 147(1):31–52. https://doi.org/10.1175/mwr-d-18-0204.1

Auvinen M, Boi S, Hellsten A, et al (2020) Study of realistic urban boundary layer turbulence with high-resolution large-eddy simulation. Atmosphere 11(2):201. https://doi.org/10.3390/atmos11020201

Bannister EJ, MacKenzie AR, Cai XM (2022) Realistic forests and the modeling of forest-atmosphere exchange. Reviews of Geophysics 60(1). https://doi.org/10.1029/2021rg000746

Basu S, Porté-Agel F (2006) Large-eddy simulation of stably stratified atmospheric boundary layer turbulence: A scale-dependent dynamic modeling approach. Journal of the Atmospheric Sciences 63(8):2074–2091. https://doi.org/10.1175/JAS3734.1

Bechmann A, Sørensen N (2010) Hybrid rans/les method for wind flow over complex terrain. Wind Energy 13:36–50. https://doi.org/10.1002/WE.346

Belcher SE, Jerram N, Hunt JCR (2003) Adjustment of a turbulent boundary layer to a canopy of roughness elements. Journal of Fluid Mechanics 488:369–398. https://doi.org/10.1017/S0022112003005019

Belcher SE, Harman IN, Finnigan JJ (2012) The wind in the willows: Flows in forest canopies in complex terrain. Annual Review of Fluid Mechanics 44(1):479–504. https://doi.org/10.1146/annurev-fluid-120710-101036, http://dx.doi.org/10.1146/annurev-fluid-120710-101036

Blunn LP, Coceal O, Nazarian N, et al (2021) Turbulence characteristics across a range of idealized urban canopy geometries. Boundary-Layer Meteorology https://doi.org/10.1007/s10546-021-00658-6

Bohrer G, Katul GG, Walko RL, et al (2009) Exploring the effects of microscale structural heterogeneity of forest canopies using large-eddy simulations. Boundary-layer meteorology 132(3):351–382. https://doi.org/10.1007/s10546-009-9404-4

Brunet Y (2020) Turbulent flow in plant canopies: Historical perspective and overview. Boundary-Layer Meteorology 177(2-3):315–364. https://doi.org/10.1007/s10546-020-00560-7

Cassiani M, Katul GG, Albertson JD (2008) The effects of canopy leaf area index on airflow across forest edges: Large-eddy simulation and analytical results. Boundary-Layer Meteorology 126(3):433–460. https://doi.org/10.1007/s10546-007-9242-1

Cheng S, Elgendi M, Lu F, et al (2021) On the wind turbine wake and forest terrain interaction. Energies https://doi.org/10.3390/en14217204

Dalpé B, Masson C (2009) Numerical simulation of wind flow near a forest edge. Journal of Wind Engineering and Industrial Aerodynamics 97(5-6):228 – 241. https://doi.org/http://dx.doi.org/10.1016/j.jweia.2009.06.008

Detto M, Katul GG, Siqueira M, et al (2008) The structure of turbulence near a tall forest edge: The backward-facing step flow analogy revisited. Ecological Applications 18(6):1420–1435

Dupont S, Brunet Y (2008) Influence of foliar density profile on canopy flow: A large-eddy simulation study. Agricultural and Forest Meteorology 148:976–990. https://doi.org/10.1016/J.AGRFORMET.2008.01.014

Dupont S, Brunet Y (2009) Coherent structures in canopy edge flow: a large-eddy simulation study. Journal of Fluid Mechanics 630:93 – 128. https://doi.org/10.1017/S0022112009006739

Dupont S, Brunet Y, Finnigan J (2008) Large-eddy simulation of turbulent flow over a forested hill: Validation and coherent structure identification. Quarterly Journal of the Royal Meteorological Society 134. https://doi.org/10.1002/QJ.328

Dupont S, Bonnefond J, Irvine MR, et al (2010a) Long-distance edge effects in a pine forest with a deep and sparse trunk space: In situ and numerical experiments. Agricultural and Forest Meteorology 151:328–344. https://doi.org/10.1016/J.AGRFORMET.2010.11.007

Dupont S, Gosselin F, Py C, et al (2010b) Modelling waving crops using large-eddy simulation: comparison with experiments and a linear stability analysis. Journal of Fluid Mechanics 652:5–44

Dupont S, Défossez P, Bonnefond J, et al (2018) How stand tree motion impacts wind dynamics during windstorms. Agricultural and Forest Meteorology https://doi.org/10.1016/J.AGRFORMET.2018.06.022

Finnigan J (2000) Turbulence in plant canopies. Annual review of fluid mechanics 32(1):519–571. https://doi.org/10.1146/annurev.fluid.32.1.519

Finnigan J, Ayotte K, Harman I, et al (2020) Boundary-layer flow over complex topography. Boundary-Layer Meteorology 177(2-3):247–313. https://doi.org/10.1007/s10546-020-00564-3

Frank C, Ruck B (2008) Numerical study of the airflow over forest clearings. Forestry 81:259–277. https://doi.org/10.1093/FORESTRY/CPN031

Irvine MR, Gardiner BA, Hill MK (1997) The evolution of turbulence across a forest edge. Boundary-Layer Meteorology 84(3):467–496. https://doi.org/10.1023/A:1000453031036

Jocher G, Fischer M, Šigut L, et al (2020) Assessing decoupling of above and below canopy air masses at a norway spruce stand in complex terrain. Agricultural and Forest Meteorology https://doi.org/10.1016/j.agrformet.2020.108149

Kanani-Sühring F, Raasch S (2015) Spatial variability of scalar concentrations and fluxes downstream of a clearing-to-forest transition: A large-eddy simulation study. Boundary-Layer Meteorology 155(1):1–27. https://doi.org/10.1007/s10546-014-9986-3

Kim WW, Menon S (1997) Application of the localized dynamic subgrid-scale model to turbulent wall-bounded flows. Technical Report AIAA-97-0210, AIAA, Reno, https://doi.org/doi:10.2514/6.1997-210

Li W, Liu CH (2021) On the flow response to an abrupt change in surface roughness. Flow, Turbulence and Combustion 108:387 – 409. https://doi.org/10.1007/s10494-021-00281-y

Li W, Liu CH, Cheng W (2020) Rans study of flows across an abrupt change in surface roughness. Journal of Applied Fluid Mechanics https://doi.org/10.36884/jafm.13.05.31017

Lin X, Chamecki M, Katul G, et al (2018) Effects of leaf area index and density on ultrafine particle deposition onto forest canopies: A les study. Atmospheric Environment https://doi.org/10.1016/J.ATMOSENV.2018.06.048

Lopes JMVP, Palma JMLM, Lopes AS (2021) Modelling the flow within forests: the canopy-related terms in the reynolds-averaged formulation. Journal of Fluid Mechanics 910. https://doi.org/10.1017/jfm.2020.927

Ma Y, Liu H, Banerjee T, et al (2020) The effects of canopy morphology on flow over a two-dimensional isolated ridge. Journal of Geophysical Research: Atmospheres 125(19). https://doi.org/10.1029/2020jd033027

Markfort CD, Porté-Agel F, Stefan HG (2014) Canopy-wake dynamics and wind sheltering effects on earth surface fluxes. Environmental Fluid Mechanics 14(3):663–697. https://doi.org/10.1007/s10652-013-9313-4

Mathey F, Cokljat D, Bertoglio JP, et al (2006) Assessment of the vortex method for large eddy simulation inlet conditions. Progress in Computational Fluid Dynamics, an International Journal 6(1-3):58–67. https://doi.org/10.1504/PCFD.2006.009483, http://www.inderscienceonline.com/doi/pdf/10.1504/PCFD.2006.009483

Patankar S (1980) Numerical Heat Transfer and Fluid Flow. Series in computational methods in mechanics and thermal sciences, Taylor & Francis

Patton EG, Katul GG (2009) Turbulent pressure and velocity perturbations induced by gentle hills covered with sparse and dense canopies. Boundary-layer meteorology 133:189–217

Philips DA, Rossi R, Iaccarino G (2013) Large-eddy simulation of passive scalar dispersion in an urban-like canopy. Journal of Fluid Mechanics 723:404–440. https://doi.org/10.1017/jfm.2013.135

Poëtte C, Gardiner B, Dupont S, et al (2017) The impact of landscape fragmentation on atmospheric flow: A wind-tunnel study. Boundary-Layer Meteorology 163. https://doi.org/10.1007/s10546-017-0238-1

Queck R, Bienert A, Maas HG, et al (2016) The turbefa field experiment–measuring the influence of a forest clearing on the turbulent wind field. Boundary-Layer Meteorology 160(3):397–423. https://doi.org/10.1007/s10546-016-0151-z

Raupach M (1987) A lagrangian analysis of scalar transfer in vegetation canopies. Quarterly Journal of the Royal Meteorological Society 113:107–120. https://doi.org/10.1002/QJ.49711347507

Raupach M, Finnigan J, Brunet Y (1996) Coherent eddies and turbulence in vegetation canopies: The mixing-layer analogy. Boundary-Layer Meteorology 78:351–382. https://doi.org/10.1007/978-94-017-0944-6_15

Raupach MR, Finnigan JJ (1995) Scale issues in boundary-layer meteorology: Surface energy balances in heterogeneous terrain. Hydrological Processes 9(5-6):589–612. https://doi.org/10.1002/hyp.3360090509

dos Reis Pinheiro LA, Mendes RCF, de Siqueira MBB, et al (2024) Turbulent flow across a clearing-forest transition: a large eddy simulation study. Journal of the Brazilian Society of Mechanical Sciences and Engineering 46(5):289. https://doi.org/10.1007/s40430-024-04834-w

Savelyev SA, Taylor PA (2005) Internal boundary layers: I. Height formulae for neutral and diabatic flows. Boundary-Layer Meteorology 115(1):1–25. https://doi.org/10.1007/s10546-004-2122-z

Schmitt A, Ament F, de Araújo AC, et al (2023) Modeling atmosphere–land interactions at a rainforest site – a case study using amazon tall tower observatory (atto) measurements and reanalysis data. Atmospheric Chemistry and Physics https://doi.org/10.5194/acp-23-9323-2023

Sharma A, García-Mayoral R (2019) Turbulent flows over dense filament canopies. J Fluid Mech 888 (2020) A2 https://doi.org/10.1017/jfm.2020.27, arXiv:1907.04020 [physics.flu-dyn]

Shaw R, Patton E (2003) Canopy element influences on resolved- and subgrid-scale energy within a large-eddy simulation. Agricultural and Forest Meteorology 115:5–17. https://doi.org/10.1016/S0168-1923(02)00165-X

Shaw RH, Schumann U (1992) Large-eddy simulation of turbulent flow above and within a forest. Boundary-Layer Meteorology 61(1):47–64. https://doi.org/10.1007/bf02033994

Sützl BS, Rooney GG, van Reeuwijk M (2021) Drag distribution in idealized heterogeneous urban environments. Boundary-Layer Meteorology 178(2):225–248. https://doi.org/10.1007/s10546-020-00567-0

Tominaga Y, Stathopoulos T (2007) Turbulent schmidt numbers for cfd analysis with various types of flowfield. Atmospheric Environment 41(37):8091–8099. https://doi.org/10.1016/j.atmosenv.2007.06.054

Venkatraman K, Hågbo TO, Buckingham S, et al (2023) Effect of different source terms and inflow direction in atmospheric boundary modeling over the complex terrain site of perdigão. Wind Energy Science https://doi.org/10.5194/wes-8-85-2023

Watanabe T (2004) Large-eddy simulation of coherent turbulence structures associated with scalar ramps over plant canopies. Boundary-Layer Meteorology 112:307–341. https://doi.org/10.1023/b:boun.0000027912.84492.54

Watanabe T, Shimoyama K, Kawashima M, et al (2020) Large-eddy simulation of neutrally-stratified turbulent flow within and above plant canopy using the central-moments-based lattice boltzmann method. Boundary-Layer Meteorology 176(1):35–60. https://doi.org/10.1007/s10546-020-00519-8

Wurps H, Steinfeld G, Heinz S (2020) Grid-resolution requirements for large-eddy simulations of the atmospheric boundary layer. Boundary-Layer Meteorology 175(2):179–201. https://doi.org/10.1007/s10546-020-00504-1

Yang B, Morse AP, Shaw RH, et al (2006) Large-eddy simulation of turbulent flow across a forest edge. part ii: Momentum and turbulent kinetic energy budgets. Boundary-Layer Meteorology 121(3):433–457. https://doi.org/10.1007/s10546-006-9083-3